Available online at www.sciencedirect.com
ScienceDirect
Surface Science 602 (2008) 960–974
SURFACE SCIENCE
www.elsevier.com/locate/susc

Water on the hydroxylated (0 0 1) surface of kaolinite: From monomer adsorption to a flat 2D wetting layer

Xiao Liang Hu, Angelos Michaelides *

Materials Simulation Laboratory, London Centre for Nanotechnology and Department of Chemistry, University College London, London WC1E 6BT, UK
Fritz-Haber-Institut der Max-Planck-Gesellschaft, Faradayweg 4-6, 14195 Berlin, Germany

Received 16 November 2007; accepted for publication 21 December 2007
Available online 2 January 2008

Abstract

In order to understand the role played by kaolinite in heterogeneous ice nucleation, an extensive density-functional theory study has been performed for water on its (0 0 1) basal plane. Water monomers at low coverage, water clusters, water bilayers and water multilayers have all been examined. The most important and interesting results from this study are: (i) water monomers bind strongly to kaolinite compared to many other substrates. In the preferred adsorption structure water accepts two H bonds from and donates one H bond to the substrate, revealing that kaolinite, like water, is amphoteric with the ability to accept and donate H bonds; (ii) clustering of adsorbed water molecules is not significantly favored. All water clusters (dimers, tetramers, and hexamers) examined are, at best, equally stable to water monomers; (iii) a 2D ice-like bilayer, with a stability matching that of ice Ih has been identified implying that water can wet kaolinite; (iv) multilayer ice growth is not favored, being considerably unstable compared to bulk ice, indicating that the water covered kaolinite surface is itself "hydrophobic". Overall we see that amphoterism of the hydroxylated surface is key to many of the interesting properties of kaolinite with regard to water adsorption and ice nucleation, revealing that the behavior of water on kaolinite is more complex and interesting than previously thought to be and highlighting the need for further theoretical and experimental work.

Keywords: Density functional calculations; Adsorption; Wetting; Water; Kaolinite

1. Introduction

The nucleation of water into ice is a familiar everyday process and one of central importance to a wide variety of disciplines such as environmental chemistry, astrophysics, and biology. However, despite being studied since antiquity, our understanding of ice nucleation is far from complete at the molecular scale. This is particularly true for so-called heterogeneously catalyzed nucleation, in which water is encouraged to nucleate through the presence of an "ice nucleating agent". Mainly this is because of the complexity of the problem: interactions between water molecules in the nascent clusters are altered by the substrate, leading to the formation of new water structures not observed in the gas phase, altered H bond strengths, dynamics and stabilities.

Great strides have been made in recent years to understand water adsorption and ice nucleation on model substrates such as metals and metal oxides. Often studied under well-defined ultra high vacuum (UHV) conditions some of these systems are rather well characterized: water–ice adlayers on Ru, Pt, and TiO_2 surfaces have, for example, been interrogated with almost every conceivable surface science probe [1–7]. Clay mineral surfaces have also been widely examined [5,6,8–10], however, less is known at the molecular level about the adsorption of water and the nucleation of ice on clay mineral surfaces. Clay minerals are important since small clay particles are one of the key types of material that encourage the nucleation of ice in the upper atmosphere [11]. A better understanding of ice

* Corresponding author.
E-mail address: angelos.michaelides@ucl.ac.uk (A. Michaelides).

0039-6028/$ - see front matter © 2007 Elsevier B.V. All rights reserved.
doi:10.1016/j.susc.2007.12.032

nucleation on such particles is greatly needed for developing and improving models of cloud formation and precipitation, and prerequisites to narrowing existing uncertainties in climate change scenarios.

Of the many clay minerals known to be effective ice nucleating agents, the mineral kaolinite ($Al_2Si_2O_5(OH)_4$) features prominently. Field studies reveal that kaolinite is often an abundant foreign material at the central nucleus of snow crystals [11]. Partly this is down to the great abundance of kaolinite in the upper atmosphere. As one of the most common minerals, produced by the chemical weathering of aluminum silicate minerals like feldspar, there is simply a lot of the stuff up there, existing as small nano- to micro-meter sized dust particles. And, partly this is down to a particular efficiency as an ice nucleating agent. The threshold temperature for ice nucleation – one criterion by which the ice nucleating ability of a material is judged – is rather high on kaolinite, at around −9 to −11 °C in the deposition mode [11].

The standard explanation for why kaolinite is an effective ice nucleating agent relates to its crystal structure, which is now well characterized [12–16]. As a layered aluminosilicate it is thought to offer perfect cleavage along its (0 0 1) basal plane exposing on each side of a finite crystal an hydroxylated and a siloxane (0 0 1) surface. The hydroxylated (0 0 1) surface is said to be hydrophilic whereas the siloxane (0 0 1) surface is said to be hydrophobic [17]. The hydrophilic hydroxylated (0 0 1) surface is further thought to be a good surface for ice nucleation since it presents a quasi-hexagonal arrangement of hydroxyl groups with O–O separations rather close to the O–O distances in the basal plane of ice Ih [11] (Fig. 1). Thus kaolinite is believed to provide a suitable template for ice nucleation in the same spirit as the anthropogenic ice nucleating agent, AgI.

Although kaolinite and water on kaolinite has been widely studied [17–21], many questions relating to the molecular level details of water adsorption and ice-like overlayer growth on kaolinite remain unanswered. Here, we make a start at addressing these issues through an extensive series of density-functional theory (DFT) calculations for water adsorption on the (0 0 1) basal plane of kaolinite. Adsorption on the hydroxylated (0 0 1) surface alone was considered with the coverage of adsorbed water ranging from monomers at low coverage to ice-like multilayers. The most important and interesting results from this study are: (i) water monomers bind strongly to kaolinite compared to many other substrates. In the preferred adsorption structure water accepts two H bonds from and donates one H bond to the substrate, revealing that kaolinite, like water, is amphoteric with the ability to accept and donate H bonds; (ii) clustering of adsorbed water molecules is not significantly favored. All water clusters (dimers, tetramers, and hexamers) examined are equally stable to or less stable than isolated monomers; (iii) a 2D ice-like bilayer, with a stability matching that of ice Ih, has been identified, implying that water can wet kaolinite; (iv) multilayer ice growth is not favored, being considerably unstable compared to bulk ice, indicating that the water covered kaolinite surface is itself hydrophobic. A key conclusion to come from this work is that we call into question the suggestion that kaolinite is a good ice nucleating agent because it provides a close lattice match to the basal plane of ice. Instead we suggest that the amphoterism of the hydroxylated substrate is key to many of the interesting properties of kaolinite with regard to water adsorption and ice nucleation.

This paper is a comprehensive account following an earlier letter [22] and the plan for the remainder is the following. In the next section we discuss the computational set-up employed. Following this in Section 3 we discuss some aspects of bulk kaolinite and in Section 4 the structure of the clean (0 0 1) surface is addressed. The main body of the results, which comprise an extensive series of calculations of water adsorption on the hydroxylated (0 0 1) surface of an isolated layer of kaolinite, are presented in Section 5 along with a discussion and some conclusions in Section 6.

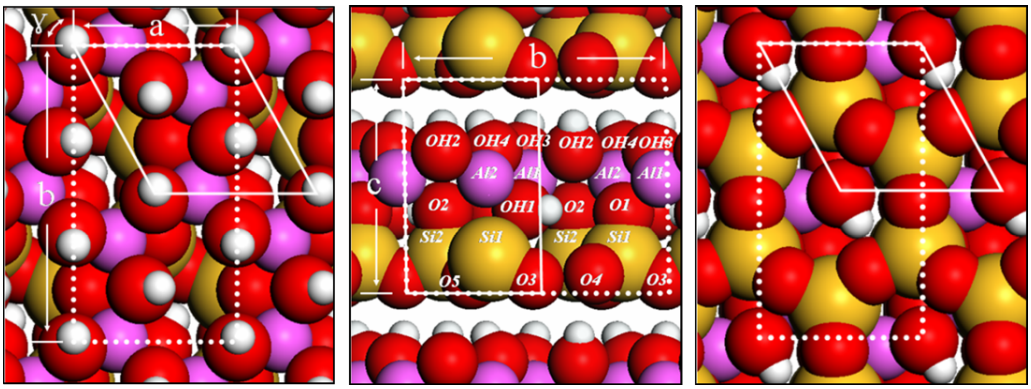

Fig. 1. Bulk kaolinite crystal structure seen from the hydroxylated (0 0 1) face (left), the side (middle), and the siloxane (0 0 1) face (right). White spheres, red (dark) spheres, purple (small gray) spheres, and dark yellow (large gray) spheres represent hydrogen, oxygen, aluminium and silicon, respectively. The dotted lines indicate the conventional unit cell of bulk kaolinite and the solid lines the primitive unit cell. The labels for the lattice parameters reported in Table 1 and atoms listed in Table 2 are also indicated. (For interpretation of the references to colour in this figure legend, the reader is referred to the web version of this article.)

2. Computational details

DFT calculations within the plane-wave pseudopotential approach, as implemented in the CASTEP code [23], have been performed. Vanderbilt ultrasoft pseudopotentials [24] generated by the CASTEP code have been used throughout. With these pseudopotentials we have chosen to use a plane-wave cutoff of 700 eV, which ensures that the total energy of each isolated atom (Si, O, Al and H) is converged to within 10 meV/atom of "absolute" convergence achieved at 1500 eV. Relative energy differences, such as cohesive energies and adsorption energies reported here are thus expected to be fully converged with respect to plane-wave cutoff. Extensive tests on the performance of the pseudopotentials for computing the atomization energies and structures of small molecules as well as bulk silicon and aluminium have been performed. These calculations, some of which are reported in Tables A1 and A2 of the Appendix, give us confidence that our chosen pseudopotentials (and cutoff) are sufficiently reliable and transferable to treat the system at hand.

The Perdew, Burke, and Ernzerhof (PBE) [25] generalized gradient approximation (GGA) has been used throughout. Recent benchmark studies on the performance of DFT-PBE for the calculation of hydrogen bond strengths and lengths for a variety of typical hydrogen-bonded system show that PBE routinely predicts hydrogen bond strengths to within an accuracy of 0.04 eV/H bond (1 kcal/mol) or better compared to the results obtained from high level quantum chemistry methods with large basis sets [26,27]. In addition, PBE yields a cohesive energy for a commonly examined model of ice Ih of -0.66 eV/H_2O [28,29], which agrees reasonably well with the experimental value of -0.61 eV/H_2O.[1] And, as we will see below, it reproduces the lattice constants and layer separation of kaolinite bulk to within, at worst, 1.4% of the experimental values.

A variety of unit cells have been used to examine bulk kaolinite and water adsorption on its (0 0 1) surface. For bulk kaolinite the conventional unit cell, $Al_4Si_4O_{10}(OH)_8$, has been employed for structure optimizations along with a $3 \times 2 \times 2$ Monkhorst–Pack $\boldsymbol{k}$ point mesh [30]. In these structure optimizations the unit cell and all atoms within it were fully allowed to relax. Test calculations with a denser $6 \times 4 \times 4$ $\boldsymbol{k}$ point mesh yield a total energy and structure identical to those with the $3 \times 2 \times 2$ $\boldsymbol{k}$ point mesh, i.e., they both have the same total energy and the volumes of the two optimized cells differ by <0.04%. Water adsorption was examined on a single layer of kaolinite in surface unit cells ranging from p(1×1) to p(3×3) and with a vacuum region between slabs of more than 10 Å. In these calculations Monkhorst–Pack $\boldsymbol{k}$ point meshes equivalent to at least $4 \times 4 \times 1$ sampling within a 1×1 unit cell were used. During structure optimizations all atoms are fully relaxed until all forces are reduced below 2×10^{-2} eV/Å.

[1] Using the Bernal-Fowler ice Ih model of Ref. [28], the PBE exchange-correlation functional, a $4 \times 4 \times 4$ Monkhorst–Pack $\boldsymbol{k}$ point mesh, ultrasoft pseudopotentials, and a plane-wave cutoff of 700 eV, a cohesive energy of -0.66 eV/H_2O is obtained. The corresponding experimental value, with contributions from zero point energy removed, is -0.61 eV/H_2O (Ref. [48]). Further, we note that our calculated zero point energy of this ice Ih model is at 0.13 eV/H_2O consistent with the experimental zero point energy (0.12 eV/H_2O).

3. Bulk kaolinite

We now address several aspects of bulk kaolinite in order to further evaluate the accuracy of our computational set-up and to familiarize the reader with this somewhat complex layered aluminosilicate. Specifically, we discuss the crystal structure and electronic structure of bulk kaolinite.

3.1. Crystal structure

As shown in Fig. 1, kaolinite is a layered aluminosilicate. Each layer is comprised of an aluminate octahedrally coordinated sublayer connected to a silicate tetrahedrally coordinated sublayer. The oxygen atoms connected exclusively to aluminium atoms exist as hydroxyl groups. Most of the hydroxyl groups are located on the (0 0 1) surface of each layer and hold adjacent layers together through hydrogen bonds. Each hydroxyl group on the basal plane is surrounded by a hexagonal arrangement of six other hydroxyl groups, which, as we will discuss below, is the textbook explanation for why kaolinite is thought to be a good material at nucleating ice [11].

The bulk crystal structure of kaolinite is reasonably well characterized thanks to X-ray [14,16] and neutron diffraction [12,13,15] experiments as well as DFT [19,20,31,32] calculations. There is, however, a minor disagreement concerning the space group: most experiments [12,14–16] report C1 (centered symmetry), but one [13] reports P1 (asymmetry). In order to address this issue of the space group we performed a series of DFT structure optimizations starting from each of the slightly different experimental crystal structures. The lowest total energy structure obtained from these calculations was that which started from the experimental structures reported by Neder et al. [16] and by Bish [15], i.e., both initial structures yield essentially identical final structures with the same total energy, the same internal bond lengths, and unit cell volumes that differ by only 0.025%. In agreement with most experimental results the structure has indeed a C1 space group.

In Tables 1 and 2 the optimized lattice constants and internal bond lengths obtained here are reported and compared to experimental results. As can be seen from Table 1 our calculated lattice constants agree well with those determined from experiment, yielding a cell volume that is only 3% larger than experiment. In particular we note that the c height of the unit cell, which is largely determined by interlayer hydrogen bonding, is within 1.4% of the experimental value, indicating that our chosen computational set-up

(exchange-correlation functional, ***k*** point mesh, pseudopotentials and cutoff energy) is suitable for describing this weak interlayer interaction. Likewise it can be seen from Table 2 that the various internal bond lengths determined here generally agree with the experimental values. We note that of the two sets of experimental data given in Table 2 we find better agreement, in terms of Al–O and Si–O bond lengths, with the X-ray diffraction data of Neder et al. [16] rather than the neutron diffraction data reported by Bish [15]. For the O–H distances, however, our calculations agree with the more reasonable values of ~1 Å to come from neutron diffraction as opposed to the unrealistically short values of ~0.75 Å reported from X-ray diffraction.

3.2. Electronic structure

The electronic structure of bulk kaolinite is now briefly discussed. In Fig. 2a the density of states (DOS) of kaolinite is displayed. It can be seen from this plot that kaolinite is an insulator with a DFT-PBE Kohn-Sham band gap of ~5.6 eV. We are not aware of any experimental reports for the (optical) band gap of kaolinite. However, it is safe

Table 1
Comparison between computed and experimental lattice parameters for the conventional unit cell of bulk kaolinte

	This work	Exp.[a]	Exp.[b]	Exp.[c]
Length (Å)				
a	5.196	5.154	5.1535	5.1490
b	9.021	8.942	8.9419	8.9335
c	7.485	7.401	7.3906	7.3844
Angle (°)				
α	91.70	91.69	91.926	91.930
β	104.72	104.61	105.046	105.042
γ	89.78	89.82	89.797	89.791
Cell volume (Å^3)	339.17	328.70	329.91	327.84

See Fig. 1 for a definition of some of the lattice parameters.
[a] Ref. [16] (X-ray single crystal diffraction experiments).
[b] Ref. [15] (low temperature (1.5 K) neutron powder diffraction experiments).
[c] Ref. [13] (neutron powder diffraction experiments).

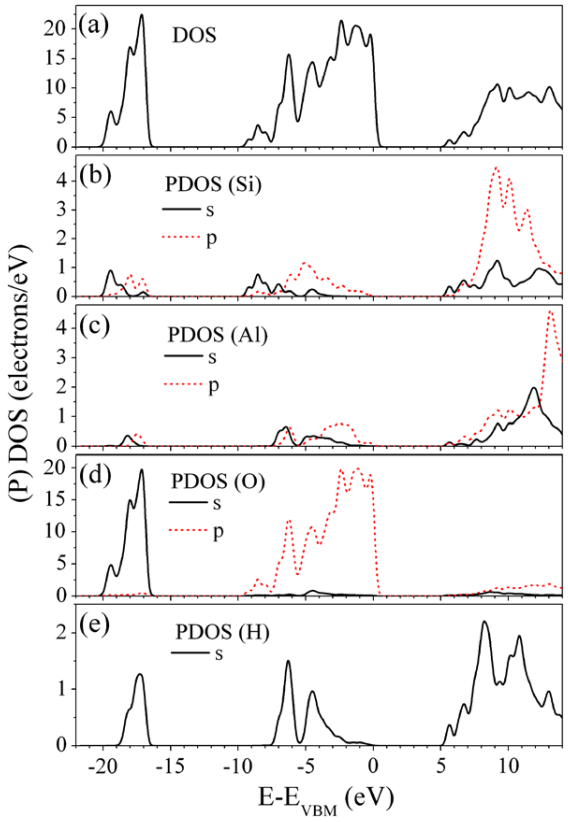

Fig. 2. DOS of bulk kaolinite (a) and PDOS of the s and p orbitals of all the Si (b), Al (c), O (d), and H (e) atoms in bulk kaolinite. The energy zero is E_{VBM}, the energy of the valence band maximum. A Gaussian broadening of 0.2 eV has been applied to all densities of states. Note that the range of the *y*-axis differs in each plot.

Table 2
Comparison between the computed and experimental internal bond lengths of bulk kaolinte

Bond	Distance (Å)			Bond	Distance (Å)		
	This work	Exp.[a]	Exp.[b]		This work	Exp.[a]	Exp.[b]
Si(1)–O(1)	1.612	1.614	1.618	Si(2)–O(2)	1.610	1.605	1.612
Si(1)–O(3)	1.634	1.620	1.611	Si(2)–O(3)	1.636	1.622	1.617
Si(1)–O(4)	1.630	1.618	1.620	Si(2)–O(4)	1.629	1.616	1.616
Si(1)–O(5)	1.637	1.628	1.619	Si(2)–O(5)	1.633	1.615	1.608
Al(1)–O(1)	1.961	1.948	1.927	Al(2)–O(1)	2.029	1.990	1.931
Al(1)–O(2)	2.038	2.001	1.930	Al(2)–O(2)	1.950	1.946	1.919
Al(1)–OH(1)	1.931	1.921	1.913	Al(2)–OH(1)	1.929	1.921	1.912
Al(1)–OH(2)	1.864	1.853	1.890	Al(2)–OH(2)	1.863	1.867	1.896
Al(1)–OH(3)	1.857	1.849	1.865	Al(2)–OH(3)	1.862	1.858	1.886
Al(1)–OH(4)	1.860	1.862	1.915	Al(2)–OH(4)	1.863	1.853	1.910
O–H(1)	0.974	0.75	0.975	O–H(3)	0.970	0.77	0.976
O–H(2)	0.969	0.76	0.982	O–H(4)	0.969	0.88	0.975

The labels given for each element are indicated in Fig. 1.
[a] Ref. [16] (X-ray single crystal diffraction experiments).
[b] Ref. [15] (low temperature (1.5 K) neutron powder diffraction experiments).

to assume that the experimental band gap will be larger than the ~5.6 eV Kohn-Sham band gap determined here. For example, the computed DFT-PBE Kohn-Sham band gaps of α-quartz (SiO_2), which resembles the silicate sublayer of kaolinite, and corundum (Al_2O_3), which resembles the aluminate sublayer of kaolinite are at ~6.0 eV and ~6.4 eV, respectively, significantly smaller (by ~30%) than the corresponding experimental (optical) band gaps. Analysis of the projected density of states (PDOS) of bulk kaolinite over the s and p orbitals of each element, as shown in Fig. 2b–e, reveals that the valence band of kaolinite is mainly comprised of oxygen p states: a filled set of p orbitals characteristic of many oxides. The band below the valence band is mostly of oxygen s character. The nature of the conduction band is less clear with s and p contributions from each of the elements and in particular significant silicon and aluminium p character.

4. (001) Surface of kaolinite

The (001) surface of kaolinite is the basal plane and the plane which kaolinite crystals predominately expose [33,34]. Thus the (001) surface and in particular the hydroxylated (001) surface is the surface of primary interest in adsorption studies. After optimizing the bulk structure, we simply cleaved the bulk along the *c*-axis through the interlayer hydrogen bonds to form its (001) surface. The structure of the single isolated layer resembles that of a layer in bulk kaolinite rather closely. All Si–O and Al–O distances, for example, are within 0.1 Å of their bulk values. Likewise the hydroxyl bond lengths remain essentially unchanged (within 0.005 Å) after cleavage along the (001) surface. The only notable difference between a layer in bulk and a layer in vacuum is that 1/3 of the surface hydroxyl groups of the isolated kaolinite layer tilt and become almost parallel to the surface. This can be seen by comparing the structure of the hydroxylated (001) surface in bulk (Fig. 1) and for an isolated surface layer (Fig. 3a). We will show below that this orientational flexibility of the OH groups at the kaolinite surface is crucial to the ability of kaolinite to support a stable water overlayer.

The cleavage energy, E_{cleave}, of this layer of kaolinite can be obtained from the following relation:

$$E_{\text{cleave}} = (E_{\text{slab}} - E_{\text{bulk}})/2 \cdot A, \tag{1}$$

where E_{slab} is the total energy of a single isolated layer of kaolinite and E_{bulk} is the total energy of a single kaolinite layer in bulk. The factor 2 in the denominator accounts for the fact that two (001) surfaces, the hydroxylated and the siloxane surfaces, are created. The area of the two dimensional surface supercell is A. The cleavage energy we obtain is 8 meV/Å^2. This corresponds to a layer–layer interaction in bulk kaolinite of ~0.36 eV/primitive cell. Since there are three interlayer hydrogen bonds in bulk kaolinite per primitive cell, this corresponds to an average interlayer hydrogen bond strength of ~0.12 eV/H bond.

We sought to consider the effect of temperature on the energetic cost to cleave a single layer of kaolinite by computing the phonon (and zero point) contribution to the cleavage free energy, $F_{\text{cleave}}(T)$. This is obtained from the relation:

$$F_{\text{cleave}}(T) = E_{\text{cleave}} + \Delta F^{\text{vib}}(T, \omega)/2 \cdot A, \tag{2}$$

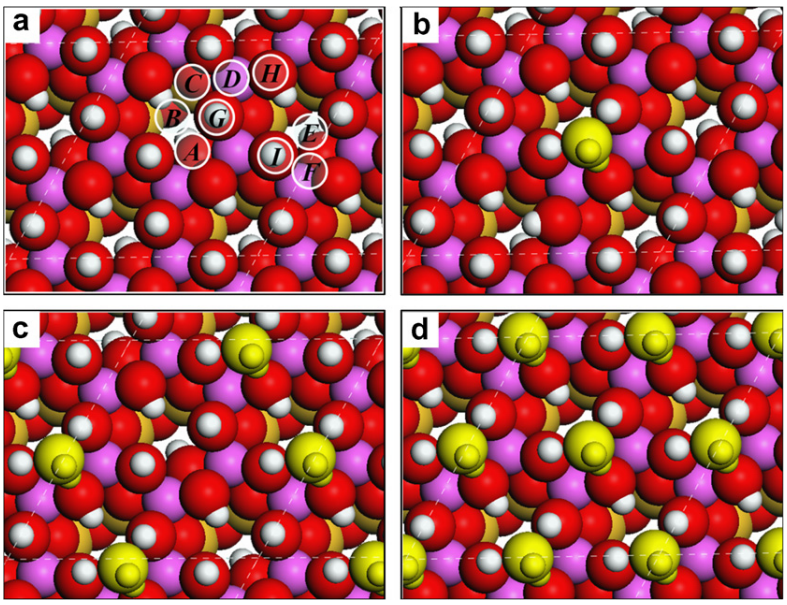

Fig. 3. (a) Top view of the clean hydroxylated (001) surface of a single layer of kaolinite with nine possible adsorption sites for water monomers indicated (A–I). (b)–(d) The most stable water monomer adsorption structures identified at 1/12, 1/6, and 1/3 ML. Here and in subsequent figures adsorbed water molecules are colored yellow (gray) for clarity. In (a)–(d) the thin dashed lines indicate the p(2 × 2) unit cell. (For interpretation of the references to colour in this figure legend, the reader is referred to the web version of this article.)

where $\Delta F^{\mathrm{vib}}(T,\omega)$ is the temperature dependent vibrational free energy contribution to $F_{\mathrm{cleave}}(T)$, given by

$$\Delta F^{\mathrm{vib}}(T,\omega) = \left(\sum (1/2)\hbar\omega_{\mathrm{slab}} - \sum (1/2)\hbar\omega_{\mathrm{bulk}}\right) + \left(\sum kT\ln(1-\exp(-\beta\hbar\omega_{\mathrm{slab}})) - \sum kT\ln(1-\exp(-\beta\hbar\omega_{\mathrm{bulk}}))\right). \quad (3)$$

The first two terms on the right hand side of Eq. (3) give the difference in zero point energies between an isolated kaolinite layer and a layer in bulk. The phonon frequencies, ω, which enter Eq. (3), were obtained in the harmonic approximation at the gamma point of the vibrational Brillouin zone through the finite displacements method. The zero point energy difference obtained with this procedure turns out to be only -40 meV/primitive cell, which corresponds to a change in the cleavage free energy of -0.8 meV/Å^2. We note that this results is a reduction in the cleavage free energy, since as one would expect, an isolated kaolinite layer has less zero point energy than a layer held in bulk. The second two terms on the right hand side give the finite temperature phonon contribution to the cleavage free energy. From Fig. 4 it can be seen that this too makes a rather small contribution, reducing the cleavage free energy by $\leqslant 1$ meV/Å^2 at all temperatures up to 1000 K. Thus, overall, we see that the energetic cost to cleave a layer of kaolinite from bulk is reasonably independent of temperature and in the range of $\sim$8 to $\sim$6 meV/Å^2.

The electronic structure of the clean single layer of kaolinite was examined. The DOS and projected DOS (not shown) were similar to those observed for bulk kaolinite. Small changes in the peak heights and widths were apparent with the center or, more precisely, the first moment of the valence band about 0.2 eV closer to the valence band maximum compared to the bulk. In addition the computed band gap is $\sim$1 eV smaller than that computed for the bulk.

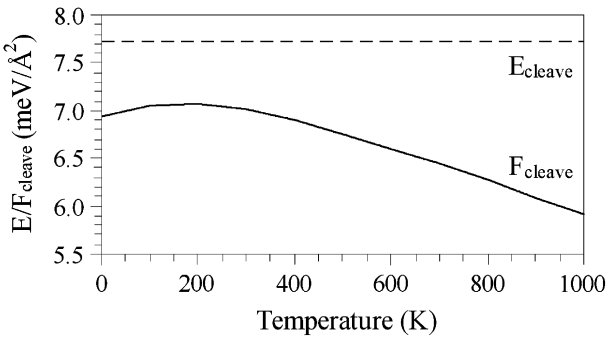

Fig. 4. The cleavage energy, E_{cleave} (Eq. (1)), of a single layer of kaolinite (dashed line) and the cleavage free energy, F_{cleave} (Eq. (2)) (solid line). At $T = 0$ K the two quantities differ by the difference in zero point energy between bulk kaolinite and a single layer of kaolinite in vacuum, which is $\sim$0.8 meV/Å^2.

5. Water adsorption

Water adsorption has been examined at a range of coverages and in a variety of structures on a single layer of kaolinite. Since previous studies [17,33] have shown that water adsorbs more weakly on the "hydrophobic" siloxane surface than it does on the "hydrophilic" hydroxylated surface, here we only examine the hydroxylated (0 0 1) surface. Adsorption energies, E_{ads}, per water are defined as

$$E_{\mathrm{ads}} = (E_{n\mathrm{H_2O/slab}} - E_{\mathrm{slab}} - n\cdot E_{\mathrm{H_2O}})/n, \quad (4)$$

where $E_{n\mathrm{H_2O/slab}}$ and E_{slab} are the total energies of an n water adsorption system and the clean surface, respectively. $E_{\mathrm{H_2O}}$ is the total energy of an isolated water molecule.[2] Within this definition a negative adsorption energy thus corresponds to an exothermic adsorption process. In order to interpret the adsorption cases explicitly and conveniently, we define a monolayer (ML) as one water molecule for every surface hydroxyl group. Thus in our most commonly employed surface supercell (Fig. 3a) one adsorbed water molecule corresponds to a coverage of 1/12 ML.

5.1. Monomer adsorption

Fig. 3a displays the hydroxylated (0 0 1) surface with the sites considered for water monomer adsorption indicated by the labels A–I. With regard to the surface hydroxyl groups we can classify four of these as threefold "hollow" sites (A–D), two as twofold "bridge" sites (E and F), and three as onefold "top" sites (G–I). All of these sites were investigated for water monomer adsorption at a coverage of 1/12 ML. During the structure optimizations the water molecules and kaolinite were fully allowed to relax and it turned out that upon optimization all the initial structures with water molecules adsorbed at top sites and one at a bridge site moved to the threefold hollow sites, which prove to be most stable sites for water monomer adsorption on this surface. At the hollow sites several similar adsorption structures, with adsorption energies all within $\sim$0.1 eV of each other, have been identified. The most stable of these is adsorption at hollow site A (Fig. 3b). At this site the monomer sits upright, in the plane of the surface normal, donating one hydrogen bond to and accepting two hydrogen bonds from the substrate. Thus kaolinite, like water, is amphoteric and able to accept and donate hydrogen bonds. The hydrogen bond the adsorbed water molecule donates is, at 1.73 Å, considerably shorter than the two hydrogen bonds it accepts, which are both $\sim$2 Å (2.00 Å and 2.03 Å). The adsorption energy of the water molecule at this site is -0.58 eV/H_2O. This adsorption energy agrees reasonably well with a previous DFT study [17] in which a binding energy of -0.64 eV was reported for hollow site adsorption.

[2] The energy of the isolated water molecule was obtained from a calculation of water in a cube of length 20 Å using only the gamma point of the Brillouin zone.

The coverage dependence of the monomer adsorption energy was then investigated by increasing the number of water monomers in the cell to two (1/6 ML) and subsequently to four (1/3 ML). At each coverage several combinations of monomer adsorption site were considered. The most stable structures identified at 1/6 ML and 1/3 ML are shown in Fig. 3c and d, respectively. In each structure all water molecules reside at the stable hollow sites A and the adsorption energies of these overlayers are both -0.57 eV/H_2O, i.e., essentially identical to the adsorption energy at 1/12 ML. Thus, the amount of water monomers on the surface has only a small effect on the adsorption energy in this coverage regime, indicating that the interaction between adjacent water molecules is weak. We note, however, that once we reach 1/3 ML we have filled all the non-connected threefold sites and there is not enough space for the adsorbed water molecules to remain isolated. At this coverage we may thus expect water cluster or extended overlayer formation. Adsorption of water clusters will be discussed in the next subsection.

It is interesting to ask to what extent zero point vibrations affect the adsorption energy of water on this surface. To this end, vibrational frequency calculations were performed for the adsorbed water monomer at 1/3 ML. The zero point energy contribution to the adsorption energy, obtained by taking the difference in the zero point energy of the adsorption system, the isolated water molecule and the clean surface, is 0.13 eV/H_2O.[3] Specifically, there is 0.13 eV/H_2O more zero point energy in the adsorption system compared to the isolated fragments, which reduces the water monomer adsorption energy from ~-0.58 eV/H_2O to ~-0.45 eV/H_2O.

5.2. Cluster and 1D chain adsorption

Since clustering tends to be facile for gas phase water molecules and water adsorbed on many types of materials, such as oxide, salt, and metal surfaces [5,35–39], we have examined the possibility of water cluster formation. Specifically, we considered water dimer, tetramer, and hexamer adsorption.

Upon moving beyond the monomer, the number of possible adsorption structures rapidly increases with cluster size and comprehensive searches of configuration space become challenging. Taking the adsorbed dimer, for example, the two water molecules in the dimer can act either as hydrogen bond donors and/or as hydrogen bond acceptors to the surface, and each water molecule may be located at hollow, bridge or top adsorption sites. Of these many possibilities we have tested fifteen different dimer structures and of those considered the most stable one identified upon optimization is the one shown in Fig. 5a. In this structure the donor water molecule in the dimer accepts two hydrogen bonds from the substrate and the other water donates one hydrogen bond to the surface. However, the adsorption energy of this structure is only -0.55 eV/H_2O, which is slightly less than the adsorption energy of a water monomer (-0.58 eV/H_2O). Thus on this surface dimer formation does not appear to be energetically favored, or, at least, we have not been able to identify any dimer structure that is more stable than two separated adsorbed water monomers. This is the opposite of what is predicted and observed on many other surfaces [5,35,39–43]. In this system the single hydrogen bond formed between the two water molecules in the dimer is not sufficient to compensate for the distortions of the two water molecules away from their optimal adsorption sites, which break hydrogen bonds to the substrate.

Similar to water dimers, fourteen different adsorbed tetramer structures have been examined, including cyclic and non-cyclic structures [35]. The most stable structure of those considered is shown in Fig. 5b. The four water molecules do not form a cyclic structure as they do in the gas phase, instead three water molecules are connected to one central water molecule, which donates one hydrogen bond to the surface. The adsorption energy of this structure is -0.58 eV/H_2O, which is equal to that of the water monomer. Thus the clustering of four water molecules does not lead to any energetic stabilization.

Adsorbed cyclic hexamers have been observed with STM on several hexagonal metal surfaces [40,42–44], and so we examined the adsorption of cyclic water hexamers here. The symmetry match of the hexamer with the substrate reduces the number of likely adsorption structures considerably but still twelve trial structures were considered. Some were built from adsorbed bilayers (below), and some hexamers considered had all six water molecules initially flat on the surface based on the structure reported on Pd(1 1 1) and Ru(0 0 0 1) [45,46]. However, the most stable adsorbed hexamer identified is one that resembles the structure of a gas phase cyclic water hexamer with three water molecules directed at the surface and the other three to the vacuum. The adsorption energy of this hexamer is -0.59 eV/H_2O and its structure is shown in Fig. 5d. Thus the adsorbed hexamer is slightly more stable than separated monomers, but the energy gain upon clustering is by no means large.

Since 1D water chains are found experimentally at, for example, steps of the Pt(1 1 1) surface [47], we have examined adsorbed 1D water chains on kaolintie. Chains with a coverage of 1/3 ML (four water molecules per cell) and 1/2 ML (six water molecules per cell) were also considered with water molecules arranged in various starting configurations. The most stable 1D chain structure, which has an adsorption energy of -0.57 eV/H_2O, is shown in Fig. 5c. It is comprised of flat water molecules and water molecules in the plane of the surface normal directed towards the

[3] Upon analysis of the vibrational modes present in the adsorption system, we find that the additional zero point energy comes from the new hindered rotations, translations, and vibrations present in the adsorption system. It is interesting to note, however, that these new modes are enough to compensate, in terms of zero point energy, for a significant softening of one of the OH stretch frequencies in the adsorbed water molecule.

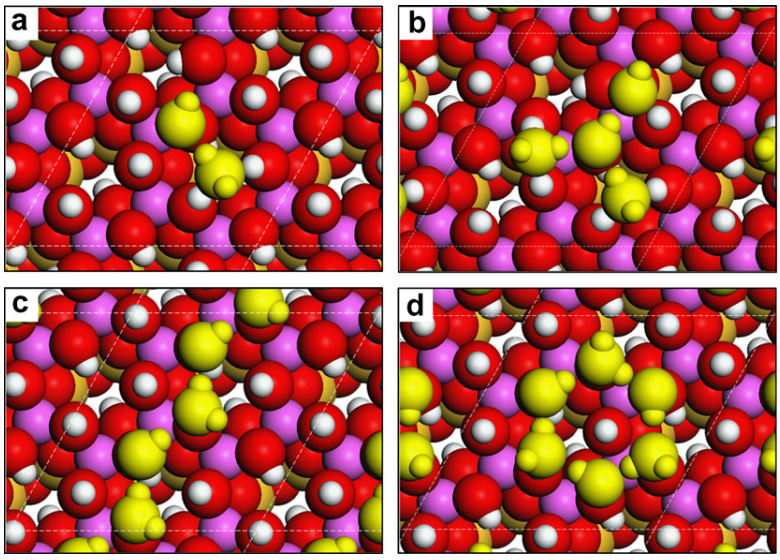

Fig. 5. Top views of the most stable structures identified for an adsorbed dimer (a), an adsorbed tetramer (b), an adsorbed 1D chain (c), and an adsorbed hexamer (d) on the hydroxylated (0 0 1) surface of a single layer of kaolinite.

surface with every water molecule being a hydrogen bond acceptor and a hydrogen bond donor. This structure is equally stable to isolated water monomers and thus not necessarily prohibited from forming on energetic grounds.

5.3. 2D overlayer adsorption

The hydroxylated (0 0 1) surface presents a quasi-hexagonal arrangement of hydroxyl groups with computed next-nearest neighbor O–O distances ranging from 2.81 to 3.41 Å. With an equivalent O–O distance of 2.71 Å in ice Ih, there is a DFT–PBE mismatch that ranges from 0.1 Å (3.7%) to 0.7 Å (25%). The corresponding experimental distances are 2.77 to 3.45 Å in bulk kaolinite [15,16] and 2.75 Å in ice Ih [48], yielding a rather similar experimental mismatch of 0.7– 25%. On this substrate we explored the possibility of adsorbing hexagonal ice-like overlayers. An extensive range of overlayer structures were considered with different coverages and various arrangements of the substrate and overlayer hexagonal meshes.[4] We discuss now a range of commensurate overlayers all with a coverage of 2/3 ML. Specifically these include a conventional ice bilayer with each water molecule directly above an hydroxyl of the substrate. In this conventional bilayer structure half the water molecules are parallel to the surface and the other half sit in the plane of the surface normal with one of their two OH groups pointing up into the vacuum (Fig. 6a). In borrowing the terminology of bilayer adsorption studies on metals we describe this as a "H-up" bilayer. A related bilayer structure can be constructed by turning the OH groups that dangle into the vacuum in the H-up bilayer toward the surface, yielding a structure known as a "H-down" bilayer (Fig. 6b) [49]. Mixed H-up plus H-down and several other commensurate but non-bilayer-like models were also considered, including mixed water–hydroxyl overlayers previously reported for water on metal surfaces [29,45,46,50,51].

The most stable overlayer identified on this surface is a H-down structure with an adsorption energy of −0.65 eV/H_2O. The adsorption energy in the H-up version of this structure is quite a bit less at −0.48 eV/H_2O.[5] From the resulting structures of the optimized bilayers it is clear why the H-down structure is favored over the H-up structure: in the H-down system there is no dangling hydrogen bonds ensuring that each water molecule is fully coordinated being involved in four hydrogen bonds.

The structure of the H-down overlayer, shown in Fig. 6b, differs significantly from a bilayer in ice, most prominently in terms of the O–O buckling between the two types of water molecules in the bilayer. In ice the O–O buckling is ∼0.96 Å, but the overlayer identified here is essentially a flat overlayer with a buckling between the two types of water molecule of ∼0.01 Å. In addition, the in-plane H_2O-H_2O distances are all between 2.90 and

[4] The structures considered included commensurate overlayers in which the hexagonal overlayer and substrate meshes were in registry, in cells ranging from p(1 × 1) to p(3 × 3) all at 2/3 ML. Non-commensurate overlayers with longer range periodicities were also considered. For example, a 6/7 ML structure in a $\sqrt{7} \times \sqrt{7}$-R(41°) cell was considered. The latter structure was examined because it had a small epitaxial mismatch of just ∼4%. However, this and other overlayers considered were all less stable than the H-down overlayer discussed. Specifically the $\sqrt{7} \times \sqrt{7}$-R(41°) overlayer yielded an adsorption energy of ∼−0.60 eV/H_2O and several $\sqrt{3} \times \sqrt{3}$-R(30°) overlayers considered yielded adsorption energies of ∼−0.58 eV/H_2O.

[5] All mixed H-up plus H-down structures considered yielded adsorption energies between the −0.65 eV/H_2O and −0.48 eV/H_2O of the pure H-up and pure H-down bilayers. The implication is that energy is gained by converting an upwardly pointing water into a down pointing water.

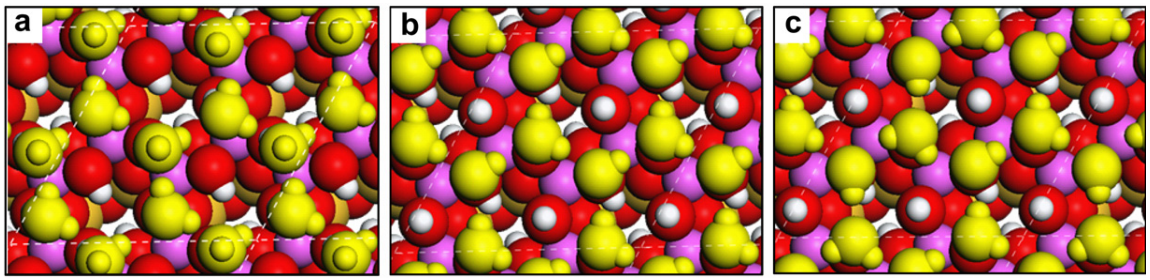

Fig. 6. Top views of some 2D overlayer adsorption structures examined at a coverage of 2/3 ML on the hydroxylated (0 0 1) surface of kaolinite. (a) is the conventional but unstable H-up overlayer. (b) is the proton ordered H-down overlayer. (c) is a partially proton disordered H-down overlayer.

3.06 Å, noticeably larger than the O–O distances in ice, which are 2.71 Å in our calculations. The range of O–O distances in the overlayer reflects an asymmetry in the substrate with two different hexagonal sets of O–O distances that the water molecules partly compensate for by displacing from the precise atop sites.

As we have said the adsorption energy of the H-down overlayer is -0.65 eV/H_2O. This is noteworthy because it is essentially identical to the computed cohesive energy of ice Ih (-0.66 eV/H_2O). It has been argued that water has the ability to wet a substrate when the adsorption energy matches or exceeds the cohesive energy of ice [29]. Thus with this criterion, and to within the accuracy of the current computational set-up, the overlayer identified here has the potential to wet kaolinite. To test this finding, we have evaluated the relative energy of ice and the H-down overlayer with several other exchange-correlation functionals (RPBE [52], PBE-WC [53], and PW91 [54]). As shown in Table 3 the conclusion that the overlayer is of comparable stability to ice is not altered, with the largest difference between adsorption energy and cohesive energy being only 0.04 eV/H_2O. We have also considered how zero point energy corrections affect the relative stability of the H-down overlayer and ice. We find that the zero point energy in the overlayer and in the ice Ih model is the same, each being 0.13 eV/H_2O.[1] Thus zero point energy does not alter the conclusion that the H-down overlayer identified here has a stability matching that of ice.

The stable H-down overlayer identified here is fully proton ordered, i.e., all the water molecules of each type (flat and down pointing) adopt the same orientations. In proton disordered structures the water molecules adopt random orientations whilst remaining consistent with the ice rules [48]. To address the question of proton disorder an additional structure in the p(2 × 2) surface cell (Fig. 6c) and two additional structures in a p(3 × 3) surface cell were calculated. However, the adsorption energies of these proton disordered structures are also -0.65 eV/H_2O. Thus, from this admittedly limited trial of partially proton disordered structures, we concluded that the adsorption energy of the H-down overlayer is not particularly sensitive to the issue of proton order.

Table 3
Adsorption energy (E_{ads}) of the H-down overlayer on the hydroxylated (0 0 1) surface and cohesive energy (E_{coh}) of ice Ih computed with several exchange-correlation functionals

	PBE	PW91	RPBE	PBE-WC
E_{ads}	−0.65	−0.67	−0.48	−0.73
E_{coh}	−0.66	−0.69	−0.49	−0.77

All values are in units of eV/H_2O.

5.4. Adsorption beyond the 2D overlayer

Having identified a stable 2D overlayer that is of comparable stability to bulk ice, we then sought to understand how facile subsequent water adsorption would be by examining the adsorption of additional water on top of the H-down (and some other) overlayer(s). Specifically, we examined the adsorption of water monomers and a second complete overlayer on top of the 2/3 ML overlayers.

Several trial structures for water monomers on top of the H-down overlayer, corresponding to a coverage of 3/4 ML, were examined. In these calculations the extra water molecules were either placed at the center of the underlying water hexagon or directly above the flat or down pointing molecules of the overlayer. Upon optimization the most stable structure identified has the extra water molecule located at a bridge-like site. At this site the additional water interrupts the H bond network of the underlying water layer by donating one hydrogen bond to one of the down pointing water molecules and accepting one hydrogen bond from one of the originally flat but now tilted water molecules. The binding energy per water in this overlayer is only marginally less than the stable H-down overlayer (-0.64 eV/H_2O).

Several structures comprised of two complete bilayers were also considered. A total of eleven different double layer structures involving changes of orientation of water in both layers were examined. However, we found that adsorption of a complete second layer of water on the first layer is energetically unfavorable. All the double bilayer structures are at least ~0.07 eV/H_2O less stable than the single H-down bilayer. Thus after the first 2D ice-like layer wets the surface, the second layer is unfavorable. Another way of saying this is that while the hydroxylated (0 0 1) surface is hydrophilic, the water covered kaolinite surface is

hydrophobic. It is most likely that this change of water adsorption energy is caused by a combination of at least two factors. First, in the H-down overlayer every water molecule is already involved in four hydrogen bonds and so does not have any dangling OH groups or dangling lone pairs with which additional water molecules could interact. Second, this applies generally to all the double bilayer structures considered, there is a lattice mismatch between the substrate and ice: A single bilayer is essentially free to compensate for any mismatch by reducing the buckling within the layer, i.e., by compressing. With more than one layer, however, hydrogen bonds must be formed between the layers. This interlayer hydrogen bonding is hampered if the bilayers flatten.

5.5. Electronic structure analysis

We now briefly address the electronic structure of the adsorption systems examined, in particular the monomer and H-down overlayer systems. To this end we consider the DOS and how the total electron densities rearrange upon adsorption. The electron density rearrangement, $\Delta\rho$, is defined as

$$\Delta\rho = \rho_{n\mathrm{H_2O/slab}} - \rho_{\mathrm{slab}} - \rho_{n\mathrm{H_2O}}, \quad (5)$$

where $\rho_{n\mathrm{H_2O/slab}}$, ρ_{slab}, and $\rho_{n\mathrm{H_2O}}$ are the electron densities of the particular water–kaolinite adsorption system under consideration, the isolated clean (0 0 1) kaolinite slab, and the isolated water molecule(s), each in the exact structure they adopt in the adsorption system.

A plot of the electron density difference for the water monomer at the most stable threefold adsorption site is shown in Fig. 7a. The nature of the electron density rearrangement displayed in Fig. 7a is characteristic of that observed before for hydrogen bonding with depletion of density around the hydrogen atoms involved in each hydrogen bond and an accumulation in density in the region of the oxygen lone pairs [35,39,55]. Clearly, when the water monomer sits at this site, three hydrogen bonds are formed, one hydrogen bond it is donating and two it is accepting. From the plot of the electron density difference there is an indication that the hydrogen bond the water monomer is donating is stronger than the two it is accepting due to the greater extent of the charge rearrangement around this bond. This is also consistent with the shorter bond length of this hydrogen bond, 1.73 Å compared to 2.00 Å and 2.03 Å.

Partial DOS plots for the monomer adsorption system are shown in Fig. 8a. Specifically, states projected onto the s and p orbitals of the water monomer are displayed. In order of increasing energy these are the $\mathbf{2a}_1$, $\mathbf{1b}_2$, $\mathbf{3a}_1$, and $\mathbf{1b}_1$ states. The splitting between these states is rather similar to what it is for a gas phase water molecule, differing from the gas phase by <0.2 eV. Upon inspection of the individual Kohn-Sham eigenstates within each peak we find only very weak character from the substrate, i.e., there is an extremely small amount of electron density mixing of the water molecule with the substrate. In other words we do not see any strong covalent bonding between the molecule and the substrate, but rather the interaction is electrostatic in nature.

Moving to the H-down overlayer, we show the electron density difference for this system in Fig. 7b. The distinct roles the two types of water molecule play in this system are immediately clear: the flat water molecule is accepting a hydrogen bond from the substrate; and the down pointing water molecule donating a hydrogen bond to the substrate. From the extent of the electron density rearrangement around each type of water molecule, it appears that their interaction with the substrate is equally strong. However, as we have said, the mode of interaction between each water molecule and the substrate differs. This can be further seen by examining the water related states in the PDOS plot for the H-down overlayer shown in Fig. 8b. Specifically, for the flat water molecule the $\mathbf{2a}_1$ and $\mathbf{1b}_2$ resonances are ~0.3 and ~0.4 eV lower in energy than they are for the down pointing water. Likewise the second closest band to the valence band maximum, $\mathbf{3a}_1$, is split into

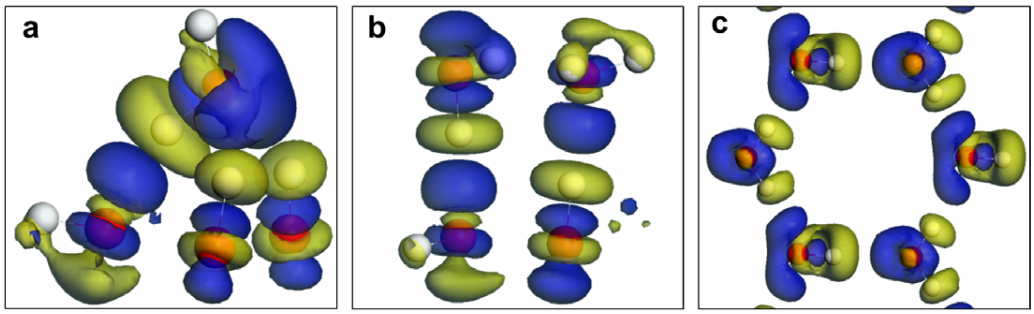

Fig. 7. Plots of electron density rearrangement for an adsorbed water monomer and water overlayer on kaolinite. Specifically (a) and (b) are side views of how the density around a single water monomer (a) and the H-down overlayer (b) rearrange upon adsorption according to Eq. (5). (c) is a top view of how the electron density rearranges within the adsorbed H-down overlayer, according to Eq. (6). (a) and (b) are designed to yield information on water–substrate bonding whereas (c) depicts water–water bonding. A constant density isosurface of 0.01 electrons/Å^3 is displayed in all plots. Blue (dark) regions indicate positive regions (electron accumulation) and yellow (bright) negative regions (electron depletion). (For interpretation of the references to colour in this figure legend, the reader is referred to the web version of this article.)

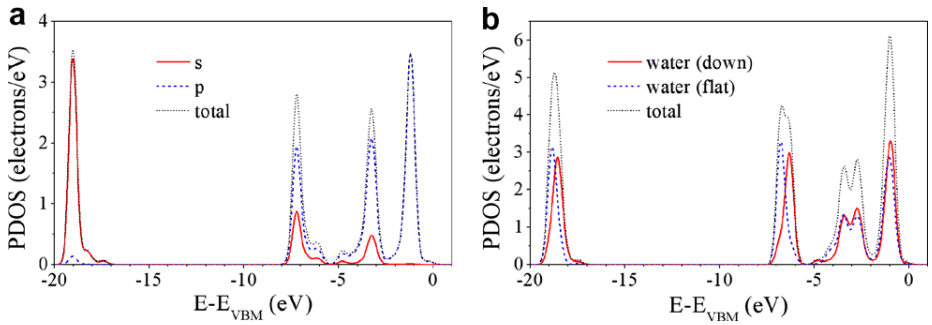

Fig. 8. PDOS on an adsorbed water monomer (a) and the H-down overlayer (b) on the hydroxylated (0 0 1) surface of kaolinite. The energy windows shown depict the four highest occupied Kohn-Sham orbitals ($\mathbf{2a}_1$, $\mathbf{1b}_2$, $\mathbf{3a}_1$, and $\mathbf{1b}_1$ from left to right) of adsorbed water. E_{VBM} is the energy of the valence band maximum.

two states caused by the differing interactions between water molecules within the overlayer and between water molecules and the substrate. As with the water monomer, inspection of the individual Kohn-Sham eigenstates contained within each peak revealed only marginal covalent mixing with the substrate.

It is interesting to ask now what the nature of the interactions between the water molecules within the overlayer are and how these compare to the water–substrate interactions. To facilitate this, a specific type of electron density rearrangmnent is defined as

$$\Delta\Delta\rho = \rho_{n\mathrm{H_2O/slab}} + \rho_{\mathrm{slab}} - \rho_{\mathrm{H_2O\_flat/slab}} - \rho_{\mathrm{H_2O\_down/slab}}, \quad (6)$$

where $\rho_{\mathrm{H_2O\_flat/slab}}$ and $\rho_{\mathrm{H_2O\_down/slab}}$ are the densities of the adsorbed flat and down pointing water molecules in the exact structure they assume in the H-down adsorption system. As before, $\rho_{n\mathrm{H_2O/slab}}$ and ρ_{slab} are the electron densities of the adsorption system and the clean substrate, respectively. The density rearrangement defined in Eq. (6) is displayed in Fig. 7c, revealing exclusively water–water interactions within the H-down overlyer. Again depletion of density on the hydrogen atoms and accumulation around the oxygen lone pairs is observed, characteristic of hydrogen bonding. Comparison of Fig. 7b and c indicates that the extent of density rearrangement is similar within the overlayer (Fig. 7c) to what it is between the overlayer and the substrate (Fig. 7b).

The plots of electron density rearrangement do not directly tell us the strength of the various hydrogen bonds in the adsorption system. A better indication of the balance between water–water and water–substrate interactions can be obtained by performing a series of interaction energy decompositions [56]. First, the interaction energy per hydrogen bond between water molecules in the overlayer, $E_{\mathrm{H_2O\text{–}H_2O}}$, is defined as

$$E_{\mathrm{H_2O\text{–}H_2O}} = 2/3 \cdot (E_{n\mathrm{H_2O/slab}} + E^*_{\mathrm{slab}} - E_{\mathrm{H_2O\_flat/slab}} - E_{\mathrm{H_2O\_down/slab}})/n, \quad (7)$$

where E^*_{slab}, $E_{\mathrm{H_2O\_flat/slab}}$, and $E_{\mathrm{H_2O\_down/slab}}$ are the total energies of the isolated clean (0 0 1) kaolinite slab, the flat water molecules in the overlayer adsorbed exclusively on the surface, and the down pointing water molecules adsorbed exclusively on the surface, each in the exact structures they adopt in the H-down overlayer. The factor 2/3 indicates that each of the two water molecules shares three hydrogen bonds in the overlayer. The water–water interaction energy we obtain from this decomposition is −0.28 eV/H bond. An analogous energy decomposition designed to reveal exclusively the interaction between a preformed H-down overlayer and the substrate, $E_{\mathrm{H_2O\text{–}slab}}$, is defined as

$$E_{\mathrm{H_2O\text{–}slab}} = (E_{n\mathrm{H_2O/slab}} - E_{n\mathrm{H_2O}} - E^*_{\mathrm{slab}})/n, \quad (8)$$

where $E_{n\mathrm{H_2O}}$ is the total energy of the isolated water overlayer in vacuum fixed in the structure it assumes when adsorbed. This water–substrate interaction energy has a value of −0.32 eV/H bond, which is slightly larger than the hydrogen bond strength between water molecules in the overlayer. Thus, in this adsorption system water molecules appear to bond more effectively with kaolinite than they do with other water molecules. This is also consistent with the computed O–O distances in the adsorption system: The O–O distances between the water molecules within the overlayer are in the interval 2.90–3.06 Å and the O–O distances between the adsorbed water molecules and the substrate are 2.72–2.81 Å.

6. Discussion and conclusions

We now summarize the energetics of the various adsorption systems examined here and place our results in the broader context of water adsorption on solid surfaces in general. To facilitate this we plot in Fig. 9 the average adsorption energy per water molecule as a function of coverage. There are several interesting features of this plot and the results described in Section 5, which we now discuss.

First, at low coverages the water adsorption energy is reasonably constant at ∼−0.57 eV/H_2O. This is a rather large value for the DFT–GGA adsorption energy of water on a solid surface: on close-packed metals, for example, water monomer adsorption energies of ∼−0.1 to −0.4 eV/H_2O are typically reported [35,39,57,58]; on NaCl values of ∼−0.3 to −0.4 eV/H_2O are found [37,38]; and on

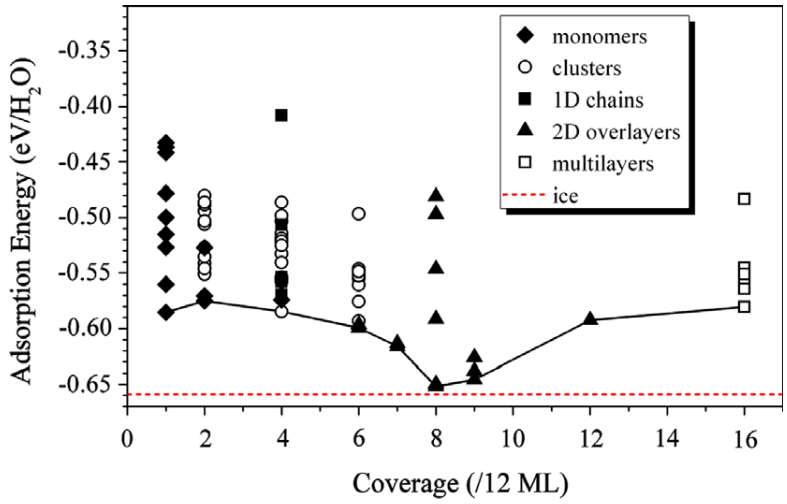

Fig. 9. Average adsorption energy per water on the hydroxylated (0 0 1) surface of kaolinite as a function of coverage. The solid line is a guide to the eye connecting the structure with largest adsorption energy at each coverage considered and the dashed line indicates the cohesive energy of ice Ih.

metal oxides, such as TiO_2, values of ~ -0.40 eV/H_2O have been reported [59–61]. Indeed, the only other report of DFT-GGA adsorption energies for water monomers as large as or larger than the value obtained here are also on hydroxylated surfaces: ~ -0.5 to -0.7 eV/H_2O on cristobalite [36] and -0.54 eV/H_2O on α-quartz [62]. Thus it is clear that an important aspect of a strong adsorption bond between water and a substrate is the presence of hydroxyl groups and the possibility of accepting and donating hydrogen bonds to and from them.

Second, we find that water clustering is not favored to any great extent. This was discussed in Section 5.2 and can be clearly seen in Fig. 9, where points corresponding to dimers, tetramers, and hexamers are equally stable to water monomers at best. Again this behavior is not common for adsorbed water and different from what is observed experimentally and predicted theoretically on metal and some oxide substrates, where clustering is strongly favored [35,39–43,63]. On the (1 1 1) surfaces of Cu, Pd, Pt, and Ni, for example, DFT calculations predict that water monomers gain 0.1–0.2 eV/H_2O by coming together to form adsorbed dimers. Likewise water molecules on some hydroxylated substrates gain 0.1–0.2 eV/H_2O by dimerization [36]. Although unusual there are, however, other substrates on which similar behavior has been predicted [38,62] notably on the hydroxylated α-quartz (0 0 0 1) surface [62].

Third, the most stable overlayer identified at any coverage is the 2/3 ML H-down overlayer. As discussed above, this overlayer has a stability similar to that of ice Ih. Again this feature of water on kaolinite differs from the behavior on many other substrates. On the low energy hexagonal surfaces of close-packed metals, for example, both the H-up and H-down overlayers tend to have adsorption energies $\geqslant 0.1$ eV/H_2O less than the cohesive energy of ice [3,56]. Likewise overlayers on other substrates often yield computed adsorption energies that are less than the cohesive energy of ice, such as on NaCl(0 0 1) which supports ice-like overlayers with computed adsorption energies of ~ -0.46 to ~ -0.57 eV/H_2O [37,38]. The application of different exchange correlation functionals, the inclusion of zero point energies, or proton disorder effects in the adsorption system does not alter the conclusion that the H-down overlayer on kaolinite is almost equally stable to bulk ice. Examination of the atomic and electronic structures in the stable H-down adsorption system provides a clear explanation for the stability of this overlayer. In it each water molecule is fully coordinated with four strong hydrogen bonds. This is made possible by the fact that kaolinite, like water, is amphoteric with the ability to accept and donate hydrogen bonds, which is possible because of the structural flexibility of the surface hydroxyl groups. This flexibility is crucial and allows the hydroxyl groups to tilt to support a stable water overlayer without dangling hydrogen bonds. Should other hydroxylated surfaces not possess such orientationally flexible hydroxyl groups then it is feasible that they may not be able to support such a stable water overlayer as kaolinite does.

Looking again at Fig. 9 several points are indicated for structures with slightly lower coverage (1/2 ML and 7/12 ML) and slightly higher coverage (3/4 ML) than that of the H-down overlayer. The latter (3/4 ML) correspond to monomers adsorbed on the H-down overlayer and the former to defective quasi-2D overlayers.[6] All of these structures are less stable than the 2/3 ML H-down overlayer, again pointing to the high stability of this overlayer with its fully coordinated water molecules.

[6] Removing a flat or an upright water molecule from the 2/3 ML H-down overlayer yielded two 7/12 ML structures. Upon optimization these structures had equal stabilities with adsorption energy of ~ -0.61 eV/H_2O. Removing two water molecules (a flat and a down pointing water molecule) yielded a 1/2 ML structure. Upon optimization this had an adsorption energy of -0.60 eV/H_2O.

Finally, we have not identified any stable double bilayer structures. All double bilayer structures examined yield adsorption energies at least 0.07 eV/H_2O less than the H-down overlayer, and are thus less stable than ice by a similar amount. Thus although a single stable wetting layer is predicted, subsequent ice growth is not favored. Essentially these results tell us that the surface of the H-down overlayer is hydrophobic. A similar conclusion has recently been made for the H-down bilayer which is thought to form on Pt(1 1 1) [64] and the OH–H_2O overlayer which also forms on Pt(1 1 1) [65]. Moreover, these results imply that the (0 0 1) basal plane of kaolinite does not support epitaxial multilayer ice growth. Thus the role played by kaolinite in heterogeneous ice nucleation is likely to be more complex than previously thought to be [11]. This may involve preferential nucleation at defective or reconstructed surfaces or nucleation on other facets. Future work by us will focus on these issues.

Acknowledgements

This work was supported by the EURYI scheme. See www.esf.org/euryi. Computer resources on the HPCx service were provided via our membership of the UK's Materials Chemistry Consortium and funded by EPSRC (portfolio grant EP/D504872).

Appendix

Here we report some of the tests performed to evaluate the accuracy of the pseudopotentials. Vanderbilt ultrasoft pseudopotentials, as generated by the built-in pseudopotential generator in the CASTEP code, were used. For users of the CASTEP code, the following strings generate the specific (PBE) pseudopotentials discussed here: "1|0.8|5|7|15|10(qc = 6.4)[]" for H; "2|1.3|5|7|15|20:21(qc = 7.5)[]" for O; "2|2.0|5|7|15|30:31: 32LGG[]" for Al; and "2|1.8|5|7|15|30:31:32LGG[]" for Si. The most important information contained in these obscure strings for each element is the following: The electronic configuration for the H pseudoatom is $1s^1$. The core radius is 0.8 a.u., the angular momentum of local channel is p, and the 1s state is treated as the valence state. The electronic configuration for the O pseudoatom is $2s^22p^4$. The core radius is 1.3 a.u., the angular momentum of local channel is d, and the 2s and 2p states are treated as the valence states. The electronic configuration for the Al pseudoatom is $3s^23p^1$. The core radius is 2.0 a.u., the angular momentum of local channel is d, and the 3s, 3p and 3d states are treated as the valence states. The electronic configuration for the Si pseudoatom is $3s^23p^2$. The core radius is 1.8 a.u., the angular momentum of local channel is d, and the 3s, 3p and 3d states are treated as the valence states.

In order to first establish an appropriate energy cutoff for calculations on our system, test calculations for a single atom in a 10 Å cubic box were performed with Γ point $\boldsymbol{k}$ sampling of the Brillouin zone. The relative energy of each of the four pseudoatoms is shown in Fig. A1. Following these tests a plane wave cutoff of 700 eV was selected, which guarantees convergence of the total energies of all elements to within 10 meV of the total energy of each element obtained with a cutoff of 1500 eV. We note that of the four pseudopotentials oxygen is the hardest. A further test calculation for oxygen with a cutoff of 3000 eV revealed that the energy difference between the total energy at 700 eV and 3000 eV was still within the very tight 10 meV convergence criteria selected here.

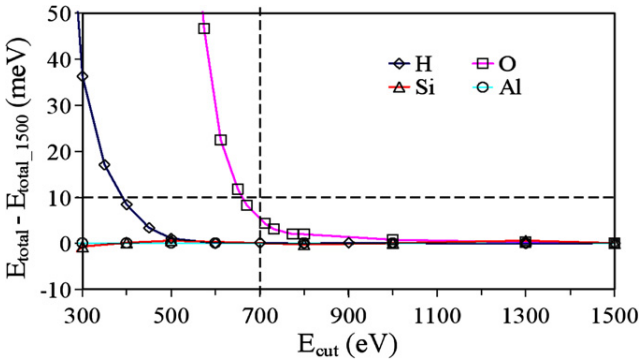

Fig. A1. Convergence of the pseudoatom total energy (E_{total}) with respect to the plane wave cutoff. All elements have been normalized to zero at a cutoff of 1500 eV (E_{total_1500}).

The quality of the pseudopotentials was tested by comparing their performance at computing the atomization energies of small molecules to the results obtained from all-electron calculations. The reference all-electron results are taken from Ref. [66], which were performed with large basis sets of Gaussian-type orbitals. Specifically an aug-cc-pVQZ basis set was used, which, for present purposes, is large enough not to suffer from significant basis set incompleteness errors. As can be seen from Table A1, the differences between the all-electron and pseudopotential results

Table A1
Comparison between pseudopotential (PP) and all-electron (AE) results for the PBE electronic atomization energy of some small molecules

Molecule	This work[a]	AE[b]	Δ (AE-PP)	Expt.[b]
H_2	4.54	4.54[c]	0.00	4.47[d]
Si_2	3.53	3.53	−0.00	3.21
Si_2H_6	22.58	22.57	−0.01	23.11
SiH_2 ($^1A_1$)	6.43	6.42	−0.01	6.68
SiH_2 ($^3B_1$)	5.72	5.72	0.00	5.68
SiH_3	9.66	9.65	−0.01	9.80
SiH_4	13.62	13.60	−0.02	14.05
H_2O_2	11.86	12.26	0.40	11.62
H_2O	9.96	10.17	0.21	10.10
O_2	5.91	6.24	0.33	5.12
OH	4.63	4.77	0.14	4.64
SiO	8.44	8.53	0.09	8.28

All values are given in eV.
[a] This work (plane-wave basis set with a cutoff energy of 700 eV).
[b] Ref. [66] (all-electron with an aug-cc-pVQZ basis set).
[c] Computed in this study with the same set-up as in Ref. [66].
[d] Experimental value from Ref. [67].

Table A2
Comparison between pseudopotential, all-electron, and experimental results for the lattice constant (a), bulk modulus (B_0) and cohesive energy (E_{coh}) of bulk aluminium and silicon

	a (Å)	B_0 (Mbar)	E_{coh} (eV/atom)
Aluminium			
This work	4.03	0.77	3.45
AE[a]	4.04	0.78	3.60
Expt.[b]	4.05	0.722	3.39
Silicon			
This work	5.46	0.89	4.57
AE[c]	5.47	0.88	4.59
Expt.[b]	5.430	0.988	4.63

[a] Ref. [68] (all-electron full-potential linearized augmented plane-wave calculations).
[b] Ref. [69].
[c] Ref. [70] (all-electron full-potential augmented plane-wave plus local orbital calculations).

are generally small. For all non-oxygen containing molecules the pseudopotentail and all-electron results agree extremely well, the differences are never more than 0.02 eV/molecule. For the oxygen containing molecules larger differences are observed, $\leqslant$0.2 eV/oxygen. This is common for oxygen pseudopotentials and for present purposes a tolerable absolute error [52].

The performance of the pseudopotentials was also tested on the properties of bulk aluminium and silicon, as listed in Table A2. All the all-electron and pseudopotental values are calculated using the PBE functional and again the agreement between the all-electron and pseudopotential results is good.

References

[1] P.A. Thiel, T.E. Madey, Surf. Sci. Rep. 7 (1987) 211.
[2] M.A. Henderson, Surf. Sci. Rep. 46 (2002) 1.
[3] C. Clay, A. Hodgson, Curr. Opin. Solid State Mater. Sci. 9 (2005) 11.
[4] A. Michaelides, Appl. Phys. A 85 (2006) 415.
[5] A. Verdaguer, G.M. Sacha, H. Bluhm, M. Salmeron, Chem. Rev. 106 (2006) 1478.
[6] G.E. Ewing, Chem. Rev. 106 (2006) 1511.
[7] G. Ketteler, S. Yamamoto, H. Bluhm, K. Andersson, D.E. Starr, D.F. Ogletree, H. Ogasawara, A. Nilsson, M. Salmeron, J. Phys. Chem. C 111 (2007) 8278.
[8] M. Odelius, M. Bernasconi, M. Parrinello, Phys. Rev. Lett. 78 (1997) 2855.
[9] P.B. Miranda, L. Xu, Y.R. Shen, M. Salmeron, Phys. Rev. Lett. 81 (1998) 5876.
[10] S.-H. Park, G. Sposito, Phys. Rev. Lett. 89 (2002) 85501.
[11] H.R. Pruppacher, J.D. Klett, Microphysics of Clouds and Precipitation– Second Revised and Enlarged Edition with an Introduction to Cloud Chemistry and Cloud Electricity, Kluwer Academic Publishers, Dordrecht, 1997, and references therein.
[12] J.M. Adams, Clays Clay Miner. 31 (1983) 352.
[13] R.A. Young, A.W. Hewat, Clays Clay Miner. 36 (1988) 225.
[14] D.L. Bish, R.B. Von Dreele, Clays Clay Miner. 37 (1989) 289.
[15] D.L. Bish, Clays Clay Miner. 41 (1993) 738.
[16] R.B. Neder, M. Burghammer, TH. Grasl, H. Schulz, A. Bram, S. Fiedler, Clays Clay Miner. 47 (1999) 487.
[17] D. Tunega, M.H. Gerzabek, H. Lischka, J. Phys. Chem. B 108 (2004) 5930.
[18] M.R. Warne, N.L. Allan, T. Cosgrove, Phys. Chem. Chem. Phys. 2 (2000) 3663.
[19] L. Benco, D. Tunega, J. Hafner, H. Lischka, J. Phys. Chem. B 105 (2001) 10812.
[20] E. Balan, A.M. Saitta, F. Mauri, G. Calas, Am. Mineral. 86 (2001) 1321.
[21] D. Tunega, L. Benco, G. Haberhauer, M.H. Gerzabek, H. Lischka, J. Phys. Chem. B 106 (2002) 11515.
[22] X.L. Hu, A. Michaelides, Surf. Sci. 601 (2007) 5378.
[23] M.D. Segall, P.J.D. Lindan, M.J. Probert, C.J. Pickard, P.J. Hasnip, S.J. Clark, M.C. Payne, J. Phys.: Condens. Matter 14 (2002) 2717; S.J. Clark, M.D. Segall, C.J. Pickard, P.J. Hasnip, M.I.J. Probert, K. Refson, M.C. Payne, Z. Kristallogr. 220 (2005) 567.
[24] D. Vanderbilt, Phys. Rev. B 41 (1990) 7892.
[25] J.P. Perdew, K. Burke, M. Ernzerhof, Phys. Rev. Lett. 77 (1996) 3865; J.P. Perdew, K. Burke, M. Ernzerhof, Phys. Rev. Lett. 78 (1997) 1396.
[26] J. Ireta, J. Neugebauer, M. Scheffler, J. Phys. Chem. A 108 (2004) 5692.
[27] B. Santra, A. Michaelides, M. Scheffler, J. Chem. Phys. 127 (2007) 184104.
[28] D.R. Hamann, Phys. Rev. B 55 (1997) R10157.
[29] P.J. Feibelman, Science 295 (2002) 99.
[30] H.J. Monkhorst, J.D. Pack, Phys. Rev. B 13 (1976) 5188.
[31] H. Sato, K. Ono, C.T. Johnston, A. Yamagishi, Am. Mineral. 89 (2004) 1581.
[32] S. Tosoni, K. Doll, P. Ugliengo, Chem. Mater. 18 (2006) 2135.
[33] M. Zbik, R.St.C. Smart, Miner. Eng. 15 (2002) 277, and references therein.
[34] W.D. Nesse, Introduction to Mineralogy, Oxford University Press, New York, 1999.
[35] A. Michaelides, Faraday Discuss. 136 (2007) 287.
[36] J. Yang, S. Meng, L. Xu, E.G. Wang, Phys. Rev. B 71 (2005) 35413.
[37] J.M. Park, J.-H. Cho, K.S. Kim, Phys. Rev. B 69 (2004) 233403.
[38] Y. Yang, S. Meng, E.G. Wang, Phys. Rev. B 74 (2006) 245409.
[39] S. Meng, E.G. Wang, S. Gao, Phys. Rev. B 69 (2004) 195404.
[40] T. Mitsui, M.K. Rose, E. Fomin, D.F. Ogletree, M. Salmeron, Science 297 (2002) 1850.
[41] V.A. Ranea, A. Michaelides, R. Ramírez, P.L. de Andres, J.A. Vergés, D.A. King, Phys. Rev. Lett. 92 (2004) 136104.
[42] K. Morgenstern, K.H. Rieder, J. Chem. Phys. 116 (2002) 5476.
[43] K. Morgenstern, J. Nieminen, Phys. Rev. Lett. 88 (2002) 066102.
[44] A. Michaelides, K. Morgenstern, Nature Mater. 6 (2007) 597.
[45] J. Cerdá, A. Michaelides, M.-L. Bocquet, P.J. Feibelman, T. Mitsui, M. Rose, E. Fomin, M. Salmeron, Phys. Rev. Lett. 93 (2004) 116101.
[46] S. Haq, C. Clay, G.R. Darling, G. Zimbitas, A. Hodgson, Phys. Rev. B 73 (2006) 115414.
[47] M. Morgenstern, T. Michely, G. Comsa, Phys. Rev. Lett. 77 (1996) 703;
M. Morgenstern, J. Mueller, T. Michely, G. Comsa, Z. Phys. Chem. (Munich) 198 (1997) 43.
[48] V.F. Petrenko, R.W. Whitworth, Physics of Ice, Oxford University Press, Oxford, 1999.
[49] H. Ogasawara, B. Brena, D. Nordlund, M. Nyberg, A. Pelmenschikov, L.G.M. Pettersson, A. Nilsson, Phys. Rev. Lett. 89 (2002) 276102.
[50] A. Michaelides, P. Hu, J. Chem. Phys. 114 (2001) 513.
[51] A. Michaelides, P. Hu, J. Am. Chem. Soc. 123 (2001) 4235.
[52] B. Hammer, L.B. Hansen, J.K. Nørskov, Phys. Rev. B. 59 (1999) 7413.
[53] Z. Wu, R.E. Cohen, Phys. Rev. B. 73 (2006) 235116.
[54] J.P. Perdew, J.A. Chevary, S.H. Vosko, K.A. Jackson, M.R. Pederson, D.J. Singh, C. Fiolhais, Phys. Rev. B. 46 (1992) 6671.
[55] A. Nilsson, H. Ogasawara, M. Cavalleri, D. Nordlund, M. Nyberg, Ph. Wernet, L.G.M. Pettersson, J. Chem. Phys. 122 (2005) 154505.
[56] A. Michaelides, A. Alavi, D.A. King, Phys. Rev. B. 69 (2004) 113404.
[57] A. Michaelides, V.A. Ranea, P.L. de Andres, D.A. King, Phys. Rev. B 69 (2004) 75409.

[58] V.A. Ranea, A. Michaelides, R. Ramírez, J.A. Vergés, P.L. de Andres, D.A. King, Phys. Rev. B 69 (2004) 205411.
[59] C.J. Zhang, P.J.D. Lindan, J. Chem. Phys. 118 (2003) 4620.
[60] P.J.D. Lindan, C.J. Zhang, Phys. Rev. B 72 (2005) 075439.
[61] S. Wendt, R. Schaub, J. Matthiesen, E.K. Vestergaard, E. Wahlström, M.D. Rasmussen, P. Thostrup, L.M. Molina, E. Lægsgaard, I. Stensgaard, B. Hammer, F. Besenbacher, Surf. Sci. 598 (2005) 226.
[62] J. Yang, E.G. Wang, Phys. Rev. B 73 (2006) 035406.
[63] D. Sebastiani, L. Delle Site, J. Chem. Theory Comput. 1 (2005) 78.
[64] G.A. Kimmel, N.G. Petrik, Z. Dohnálek, B.D. Kay, Phys. Rev. Lett. 95 (2005) 166102.
[65] G. Zimbitas, M.E. Gallagher, G.R. Darling, A. Hodgson, J. Chem. Phys., in press.
[66] J. Paier, R. Hirschl, M. Marsman, G. Kresse, J. Chem. Phys. 122 (2005) 234102.
[67] CRC Handbook of Chemistry and Physics, 88th ed., CRC, Boca Raton, FL, 2007–2008.
[68] J.L.F. Da Silva, C. Stampfl, M. Scheffler, Surf. Sci. 600 (2006) 703.
[69] C. Kittel, Introduction to Solid State Physics, eighth ed., Wiley, New York, 2005.
[70] M. Hortamani, Theory of adsorption, diffusion and spin-polarization of Mn on Si(0 0 1) and Si(1 1 1) substrates, FU Berlin, Ph.D. thesis, 2006.